







ARTICLE

Open Access

# Pulsed laser-assisted direct fabrication of $\text{Mo}_x\text{W}_{1-x}\text{S}_2$ alloy-based flexible strain sensors with superior performance for high-temperature applications

Kexin Wang<sup>1</sup>, Hanxin Wang<sup>1</sup> , Xiaoshan Zhang<sup>1</sup>, Yingzhe Li<sup>1</sup> , Yilin Zhou<sup>1</sup>, Manzhang Xu<sup>1,2,3</sup> , Weiwei Li<sup>1,2,3</sup> ✉, Lu Zheng<sup>1,2,3</sup> ✉, Xuewen Wang<sup>1,2,3,4</sup> ✉ and Wei Huang<sup>1,2,3,4,5,6</sup>

## Abstract

Flexible strain sensors with high sensitivity and stability at high temperatures are significantly desirable for their accurate and long-term signal detection in wearable devices, environment monitoring, and aerospace electronics. Despite the considerable efforts in materials development and structural design, it remains a challenge to develop highly sensitive, flexible strain sensors operating at high temperatures due to the trade-off between sensitivity and stability for the representative sensing materials. Herein, we develop a high-temperature flexible sensor using  $\text{Mo}_x\text{W}_{1-x}\text{S}_2$  alloy films. A pulsed laser is introduced to directly synthesize  $\text{Mo}_x\text{W}_{1-x}\text{S}_2$  patterns with controllable compositions and physical parameters, enabling the realization of flexible sensors without photolithography or transfer procedures. The resultant flexible sensors exhibit a high gauge factor of 97.4, a low strain detection of 4.9  $\mu\epsilon$ , and strong tolerance to a temperature of 500 °C. Owing to its superior performance, we develop a wireless acoustic recognition system to distinguish tiny strain signals of tuning forks with a vibration frequency up to 128 Hz under extreme temperature conditions. The laser method for the direct fabrication of  $\text{Mo}_x\text{W}_{1-x}\text{S}_2$  alloy-based flexible sensors holds great potential in the precise detection of strain signals from complex structures at high temperatures.

## Introduction

Thin-film flexible sensors operating at high temperatures have garnered considerable attention in both industry and fundamental research fields due to the highly conformal to complex surfaces for high-accuracy detection of temperature, strain, and pressure signals<sup>1</sup>. Additionally, the miniaturization and light weight of these sensors benefit the significant reduction in size and volume<sup>2,3</sup>, demonstrating impressive potential in soft

robotics, chemical industry, and aerospace. Therefore, extensive work has been conducted to explore novel sensing materials and construct unique structures to enhance the thermal tolerance of flexible sensors for the precise discrimination of subtle variations in temperature and strains in harsh environments. In this regard, noble metals including Pt<sup>4,5</sup>, Au, and AgPd<sup>6,7</sup> are widely used for high-temperature sensing applications due to their superior electrical conductivity and high stability over a temperature of 800 °C. However, these sensors typically have limited resistance changes to temperature and strain, resulting in a relatively low sensitivity. Metal oxides, such as indium tin oxides and indium oxides exhibit improved sensitivity over a broad temperature regime<sup>8,9</sup>. Still, their large resistance drift and slow response hindered further applications. Several novel nanomaterials, such as low-dimensional carbons<sup>10–12</sup>, metal-organic frameworks<sup>13,14</sup>,

Correspondence: Weiwei Li ([iamwwli@nwpu.edu.cn](mailto:iamwwli@nwpu.edu.cn)) or Lu Zheng ([iamlzheng@nwpu.edu.cn](mailto:iamlzheng@nwpu.edu.cn)) or Xuewen Wang ([iamxwwang@nwpu.edu.cn](mailto:iamxwwang@nwpu.edu.cn))

<sup>1</sup>State Key Laboratory of Flexible Electronics (LoFE) & Institute of Flexible Electronics (IFE), Northwestern Polytechnical University, Xi'an 710072, China

<sup>2</sup>Shaanxi Key Laboratory of Flexible Electronics, Northwestern Polytechnical University, Xi'an 710072, China

Full list of author information is available at the end of the article

These authors contributed equally: Kexin Wang, Hanxin Wang, Xiaoshan Zhang

© The Author(s) 2025



**Open Access** This article is licensed under a Creative Commons Attribution-NonCommercial-NoDerivatives 4.0 International License, which permits any non-commercial use, sharing, distribution and reproduction in any medium or format, as long as you give appropriate credit to the original author(s) and the source, provide a link to the Creative Commons licence, and indicate if you modified the licensed material. You do not have permission under this licence to share adapted material derived from this article or parts of it. The images or other third party material in this article are included in the article's Creative Commons licence, unless indicated otherwise in a credit line to the material. If material is not included in the article's Creative Commons licence and your intended use is not permitted by statutory regulation or exceeds the permitted use, you will need to obtain permission directly from the copyright holder. To view a copy of this licence, visit <http://creativecommons.org/licenses/by-nc-nd/4.0/>.

and thermoelectric fabrics<sup>15</sup> have also been adopted as sensing materials for flexible sensors with the achievements of enhanced conformability, stretchability, and even dual-mode sensing. However, their environmental stability and processability are required for further study. Despite the considerable efforts, it remains a challenge to develop flexible strain sensors with high sensitivity, stability, fast response, and easy processability for high-temperature applications.

Recently, transition metal dichalcogenides (TMDs) and their alloys have proved to be one of the promising materials in high-performance flexible sensing electronics<sup>16–18</sup>. Their layered structure with sub-nanoscale thickness allows superior flexibility and stability under mechanical bending<sup>19</sup>. Additionally, ultra-fast response and high sensitivity to optoelectronic<sup>20–22</sup> and thermal stimuli<sup>23</sup> are achieved in MoS<sub>2</sub> and other TMDs-based flexible electronics<sup>24</sup>. However, up to now, most works focused on the synthesis and growth of TMD and their alloys with limited investigations on the ultrathin films with optimal structural design for potentials in flexible mechanical sensors. Although prior works on MoS<sub>2</sub> flexible sensors have indicated high gauge factor (GF) of about 50<sup>25,26</sup> and temperature coefficient of resistance<sup>23,27</sup>, their sensing performance and potential in high-temperature applications remain unexplored.

Here, we use continuous Mo<sub>x</sub>W<sub>1-x</sub>S<sub>2</sub> ( $0 \leq x \leq 1$ , steps of 0.1) films with a nanoscale thickness as sensitive materials for flexible strain sensors. Through a highly programmable direct laser writing approach, we achieve custom Mo<sub>x</sub>W<sub>1-x</sub>S<sub>2</sub> patterns with controllable compositions, thickness, and physical dimensions. In situ decomposition of precursors under high laser energy enables the conversion of precursors to MoS<sub>2</sub>, WS<sub>2</sub>, and their alloys (Mo<sub>x</sub>W<sub>1-x</sub>S<sub>2</sub>), allowing the direct fabrication of flexible sensors without complicated photolithography procedures and transferring processes. The flexible sensors can distinguish subtle strains with a minimum microstrain of 4.9, an ultrahigh sensitivity of 97.4, and high stability at a temperature of 500 °C. The superior sensing characteristic of the developed Mo<sub>x</sub>W<sub>1-x</sub>S<sub>2</sub> sensors can be utilized to identify tidy strain signals at high temperatures for acoustic recognition and diagnosis applications.

## Materials and methods

### Synthesis of Mo<sub>x</sub>W<sub>1-x</sub>S<sub>2</sub> alloy films

A certain mass of (NH<sub>4</sub>)<sub>2</sub>MoS<sub>4</sub> and (NH<sub>4</sub>)<sub>2</sub>WS<sub>4</sub> was dissolved in a solvent mixture containing 5 mL of DMF, 4 mL of ethanolamine, and 4 mL of n-butylamine. The precursor solution was magnetically stirred at 1500 rpm for 120 min, followed by ultrasonic treatment for 60 min. The mica substrate was cleaned using UV/ozone plasma for 5 min. Then, the precursor solution was spin-coated on the mica substrate using a gradient program of

500 rpm for 10 s and 1500 rpm for 5 s. The mica substrate was then placed on a hot plate to bake at 60 °C for 5 min and then at 130 °C for 3 min.

The Mo<sub>x</sub>W<sub>1-x</sub>S<sub>2</sub> alloy films were synthesized using a commercial laser direct writing system (Xi'an Langrui Laser Technology Co., Ltd.) with a fiber laser wavelength of 1.06 μm and a spot size of about 22 μm. A piece of mica substrate with precursor solution was placed face-up on a 285 nm SiO<sub>2</sub>/Si substrate, and another piece of mica with precursor solution was placed face-down on the previous mica substrate. A programmable pattern is struck with EZCAD laser marking software under a 70 mm square field mirror. The detailed parameters of the laser writing are as follows: laser power, 3 W (15%), scanning speed, 1000 mm/s, scanning frequency, 200 kHz, and energy density, 3.9 J/cm<sup>2</sup>. After the laser writing, the Mo<sub>x</sub>W<sub>1-x</sub>S<sub>2</sub> alloy films can be obtained on the upper and lower mica surfaces, but the material on the upper mica surface has higher quality. After laser writing, the mica substrate is washed in a mixture of DMF and ethanolamine at 50 °C for 180 s to remove residual precursors. Finally, the substrate was dried at 210 °C for 5 min, and the Mo<sub>x</sub>W<sub>1-x</sub>S<sub>2</sub> pattern was left on the mica substrate.

### Materials characterization

The morphology and microstructures of the Mo<sub>x</sub>W<sub>1-x</sub>S<sub>2</sub> film were characterized using optical microscopy (Nexcope NM910), Raman (WITEC Alpha 300 R), AFM (Asylum Research Cypher S), XPS (Thermo SCIENTIFIC ESCALAB 250Xi), SEM (Gemini SEM 300), and TEM (FEI Talos F200X TEM). The Raman characterization was conducted using a 532 nm laser calibrated with a Raman peak of Si at 520 cm<sup>-1</sup>. The binding energy of the XPS results was corrected by assigning a value of 284.8 eV to the adventitious C 1 s line.

### Fabrication of Mo<sub>x</sub>W<sub>1-x</sub>S<sub>2</sub> sensors

A Mo<sub>x</sub>W<sub>1-x</sub>S<sub>2</sub> alloy film (typical area of 8 mm × 10 mm) was synthesized on a mica substrate. A 300 nm-thick Pt electrode was deposited on the mica substrate using a magnetron sputtering system (DM400-III, Hefei Poly Vacuum Science and Technology Ltd., China). The mask plate and the mica substrate were sequentially placed into the designed integrated recess before sputtering, and the recess was placed into the magnetron sputtering system. The electrode pattern corresponding to the mask plate pattern is left on the mica substrate surface by the mask plate masking effect during plating. The DC target was adopted and the coating power and time were set to 40 W and 1800 s.

### Electromechanical behavior characterization

A homemade high-temperature sensing test system was designed to evaluate the strain performance of the sensor

at high temperatures. A stepper motor was used to control the strain applied to the sensor. A LabVIEW program was developed for data acquisition based on a source meter (Keithley 2450, Tektronix).

### Calculation of strain for $\text{Mo}_x\text{W}_{1-x}\text{S}_2$ strain sensor

The bending process of the strain sensor can be simplified as a cantilever model (Fig. S1, Supporting Information). The moment of inertia ( $I$ ) and the corresponding strain ( $\varepsilon$ ) can be expressed using the following equations:

$$I = \frac{1}{12}wt^3 \quad (1)$$

$$\varepsilon = \frac{\sigma}{E} = \frac{Mc}{EI} = \frac{6Fd}{Ewt^2} \quad (2)$$

where  $w$ ,  $t$ , and  $E$  are the width, thickness, and Young's modulus of the device,  $M$  is the bending moment,  $c$  is the distance between the neutral axis and the surface,  $F$  is the applied force, and  $d$  is the distance of the material to the free end of the cantilever.

The displacement of the cantilever at the position  $x$  under force ( $\Delta L(x)$ ) is denoted as:

$$\Delta L(x) = \frac{F}{6EI}(3Lx^2 - x^3) \quad (3)$$

where  $L$  is the length of the substrate. Then, we can obtain the relationship between strain and the displacement of the cantilever under bending by solving Eqs. (1)–(3).

## Results

### Fabrication process of $\text{Mo}_x\text{W}_{1-x}\text{S}_2$ strain sensors

The fabrication process of the  $\text{Mo}_x\text{W}_{1-x}\text{S}_2$ -based flexible sensors is illustrated in Fig. 1a.  $\text{Mo}_x\text{W}_{1-x}\text{S}_2$  films were synthesized by a facile direct laser writing method at room temperature and ambient pressure. In brief, the precursor solutions containing a certain proportion of  $(\text{NH}_4)_2\text{MoS}_4$  and  $(\text{NH}_4)_2\text{WS}_4$  (details in the Experimental Section, and Fig. S2, Supporting Information) were spin-coated on the ozone-treated mica substrate and then baked to allow the evaporation of organic solvents. The laser writing process endows the direct realization of sensors with arbitrary shapes without complicated photolithography procedures or transfer processes. We then adopted a 1.06  $\mu\text{m}$  fiber laser to two face-to-face mica substrates with the precursor films for direct laser writing (Fig. S3, Supporting Information). Patterned  $\text{Mo}_x\text{W}_{1-x}\text{S}_2$  films were obtained on the mica substrate through the thermal decomposition and pyrolysis of the precursors (Fig. S4, Supporting Information). Note that a rising process was required to remove the residual precursors in the nontreated area. After removing the residual precursors, we can visualize the patterned  $\text{Mo}_x\text{W}_{1-x}\text{S}_2$  films under an optical microscope (OM) and in scanning electron microscope (SEM) image. Figure 1b, c show that the bright and dark field OM images for a typical film, revealing clear edges with continuous and homogeneous structures over a large area, which is also obverse for the  $\text{Mo}_x\text{W}_{1-x}\text{S}_2$  films with different Mo compositions ( $x = 0-1$ ) (Fig. S5, Supporting Information). The microstructure is also confirmed by the

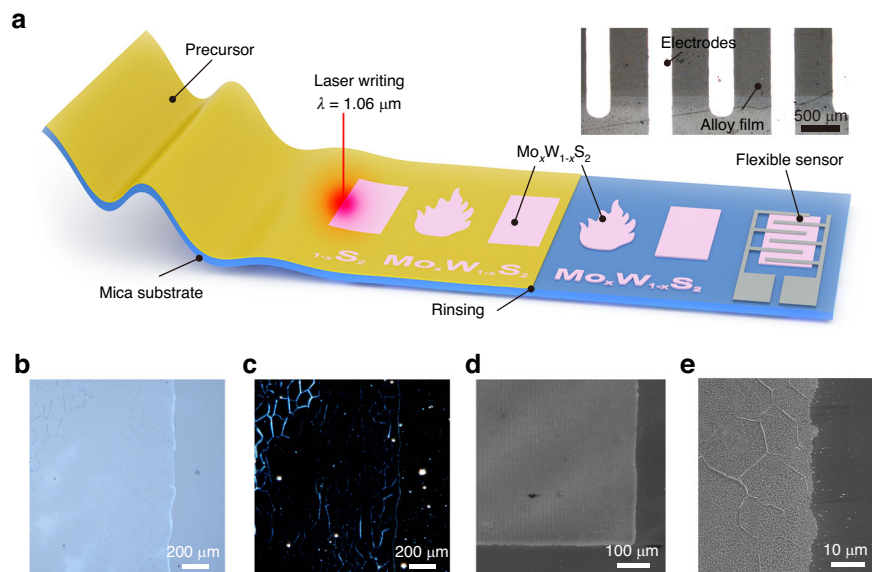


**Fig. 1** Fabrication of  $\text{Mo}_x\text{W}_{1-x}\text{S}_2$ -based flexible sensors. **a** Schematic illustration of the procedures for the fabrication, including precursor deposition on mica, direct laser writing, rinsing, and electrode sputtering. Inset shows an optical image of the alloy film and electrode. **b, c** bright field and dark field OM images, **d, e** SEM images of  $\text{Mo}_{0.2}\text{W}_{0.8}\text{S}_2$  film

SEM image (Fig. 1d), whereas a continuous film with clear edge and patterned structure is observed. It should be noted that the edges of the  $\text{Mo}_x\text{W}_{1-x}\text{S}_2$  films are not sharp and straight, with some irregular arcs, which can be ascribed to the circular spot of the laser beam. Additionally, the obtained films have some wrinkles and overlapped folds, as shown in Fig. 1e. The size of these geometric polygons is about 10  $\mu\text{m}$ , while the width of the wrinkles is about 700 nm. The distribution of the wrinkles is roughly consistent with the mica, which may be caused by the lattice orientation of the mica substrate.

We then deposit a 300 nm-thick Pt electrode on the  $\text{Mo}_x\text{W}_{1-x}\text{S}_2$  patterns using a magnetron sputtering system to complete the fabrication of the  $\text{Mo}_x\text{W}_{1-x}\text{S}_2$ -based flexible sensors. The dimensions of the  $\text{Mo}_x\text{W}_{1-x}\text{S}_2$  patterns and the electrodes are 10 mm  $\times$  5 mm and 12 mm  $\times$  8 mm, respectively. Note that the proposed strategy is highly scalable, as confirmed by the production of ten devices in a single batch (Fig. S6a, Supporting Information). Additionally, with the optimized laser parameters, we can achieve relatively high reproducibility of these sensors, whereas the electrical resistances of these sensors are from 22.7 to 29.6 M $\Omega$  with a standard deviation of 2.7 M $\Omega$ . Owing to the ultra-thin thickness of the  $\text{Mo}_x\text{W}_{1-x}\text{S}_2$  films and the microscale mica substrate, the resultant sensors are highly flexible (Fig. S6b, Supporting

Information), which can be bent with a bending radius of about 10 mm without any noticeable delamination or failure (Fig. S7, Supporting Information). It is also noted that the composition of the  $\text{Mo}_x\text{W}_{1-x}\text{S}_2$  (i.e.,  $\text{MoS}_2$ ,  $\text{WS}_2$ , and their alloys) can be facily controlled by tailoring the proportion of the precursors. Additionally,  $\text{Mo}_x\text{W}_{1-x}\text{S}_2$  patterns or continuous films are highly programmable, enabling the customized design for electronic devices or circuits.

### Characterizations of $\text{Mo}_x\text{W}_{1-x}\text{S}_2$ films

An atomic force microscope (AFM) has been adopted to evaluate the thickness of the as-prepared film. As shown in Fig. 2a, the  $\text{Mo}_x\text{W}_{1-x}\text{S}_2$  film exhibits a typical thickness of about 12 nm and an average roughness of about 2.8 nm, confirming the ultrathin nanofilms with smooth surface and uniform and homogeneous thickness. Apart from the flat  $\text{Mo}_x\text{W}_{1-x}\text{S}_2$  films, some grain boundaries with a height of about 14 nm can be observed (Fig. S8, Supporting Information), which is consistent with the OM and SEM images in Fig. 1c and e.

We further use transmission electron microscopy (TEM) to analyze the crystalline structure and quality of the  $\text{Mo}_x\text{W}_{1-x}\text{S}_2$  film. The TEM image confirms the large-area, continuous, and microcrack-free film (Fig. 2b). The energy dispersive X-ray spectroscopy (EDXS) is also

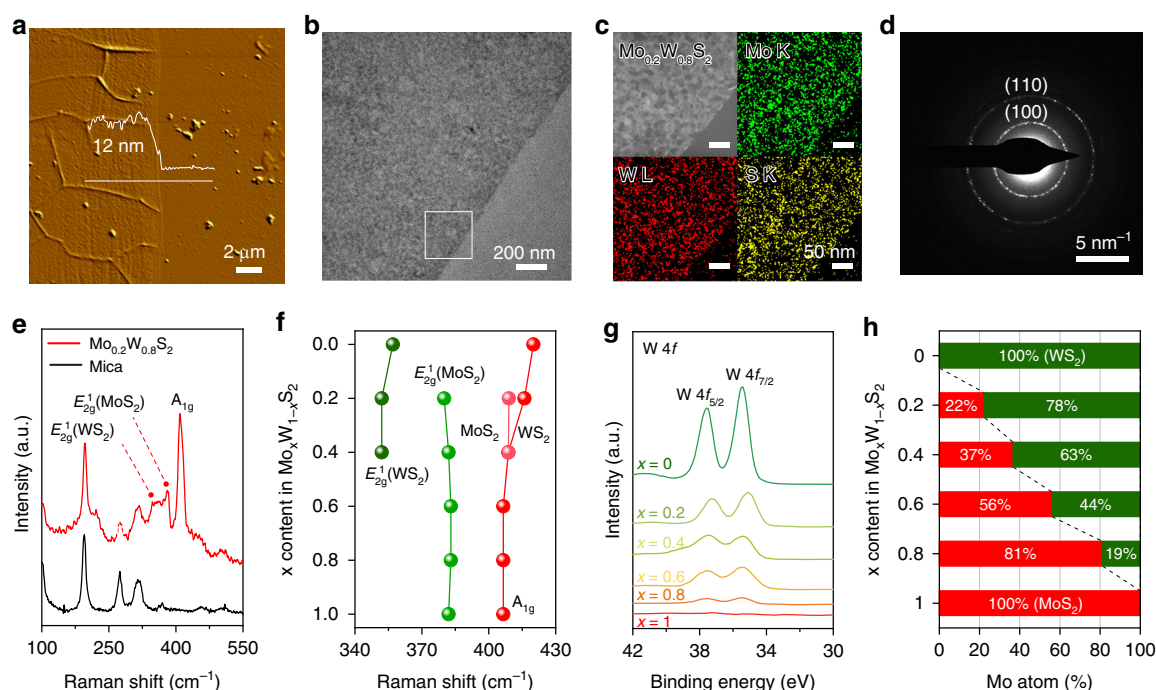


**Fig. 2** Controllable synthesis and characterizations of  $\text{Mo}_x\text{W}_{1-x}\text{S}_2$  films. **a** AFM, and **b** TEM image of  $\text{Mo}_0.2\text{W}_0.8\text{S}_2$  film. **c** EDXS mappings of  $\text{Mo}_0.2\text{W}_0.8\text{S}_2$  film. **d** SAED pattern of  $\text{Mo}_0.2\text{W}_0.8\text{S}_2$  film. **e** Raman spectra of  $\text{Mo}_0.2\text{W}_0.8\text{S}_2$  film and mica. **f** The composition-dependent Raman shift of the  $\text{Mo}_x\text{W}_{1-x}\text{S}_2$  films and the corresponding vibration modes. **g** Composition-dependent high-resolution XPS spectra of W 4f spectra of the  $\text{Mo}_x\text{W}_{1-x}\text{S}_2$  films. **h** The extracted stoichiometric ratios of the Mo and W from the XPS results



conducted to investigate the element distribution. The EDXS mappings reveal that the Mo, W, and S elements are well-distributed in the film (Fig. 2c), indicating the uniformity of the  $\text{Mo}_x\text{W}_{1-x}\text{S}_2$  films. The selected area electron diffraction (SAED) result indicated the polycrystalline structure of the  $\text{Mo}_x\text{W}_{1-x}\text{S}_2$  films (Fig. 2d), consistent with the synthesized TMDCs using the laser-assistance method<sup>28</sup>. The typical Raman spectrum of the  $\text{Mo}_x\text{W}_{1-x}\text{S}_2$  film is shown in Figs. 2e and S9, Supporting Information. As noticed, the mica shows typical Raman peaks located in 195, 275, and 314  $\text{cm}^{-1}$ . Apart from the peaks of the mica, the  $A_{1g}$  and  $E_{2g}^1$  modes of the  $\text{Mo}_x\text{W}_{1-x}\text{S}_2$  films with Raman peaks at around 340–430  $\text{cm}^{-1}$  are observed. All these results confirmed the synthesis of  $\text{Mo}_x\text{W}_{1-x}\text{S}_2$  nanofilms with large area and high quality.

As mentioned,  $\text{Mo}_x\text{W}_{1-x}\text{S}_2$  with controllable composition can be easily obtained using our laser-assistant pyrolysis method. The  $x$  content in the  $\text{Mo}_x\text{W}_{1-x}\text{S}_2$  was determined by the molar ratio of  $(\text{NH}_4)_2\text{MoS}_4$  and  $(\text{NH}_4)_2\text{WS}_4$ . The Raman spectra of the  $\text{Mo}_x\text{W}_{1-x}\text{S}_2$  films with various Mo concentrations were measured to examine the composition-dependent lattice vibration modes. As shown in Figs. 2f and S10a in Supporting Information, with the composition of  $x$  increased from 0 to 1, the  $\text{Mo}_x\text{W}_{1-x}\text{S}_2$  films evolved from  $\text{WS}_2$  to  $\text{MoS}_2$ , verified by the Raman shift. In specific, for  $x = 1$ , there are two typical Raman peaks around 382 and 407  $\text{cm}^{-1}$ , corresponding to the  $E_{2g}^1$  and  $A_{1g}$  vibrational modes of  $\text{MoS}_2$ <sup>24,29</sup>. When  $x$  is 0, two typical Raman peaks are located at 356 and 420  $\text{cm}^{-1}$ , assigned to the  $E_{2g}^1$  and  $A_{1g}$  vibrational modes of  $\text{WS}_2$ <sup>30</sup>. With the composition of  $x$  decreased from 1 to 0, the  $E_{2g}^1(\text{MoS}_2)$  peak is blue-shifted from 382  $\text{cm}^{-1}$  to 380  $\text{cm}^{-1}$ , and the  $E_{2g}^1(\text{WS}_2)$  peak is red-shifted from 352  $\text{cm}^{-1}$  to 357  $\text{cm}^{-1}$ , which can be attributed to the effect of the heavy W atoms on the high-frequency vibration<sup>31,32</sup>. Besides, when the composition of  $x$  decreased from 1 to 0, there was a redshift in the  $A_{1g}$  peak from 407  $\text{cm}^{-1}$  to 420  $\text{cm}^{-1}$ , and it was split into two peaks of  $\text{MoS}_2$  and  $\text{WS}_2$ , revealing the transformation from  $\text{MoS}_2$  to  $\text{WS}_2$ .

The X-ray photoelectron spectroscopy (XPS) spectra have been carried out to analyze the chemical composition of the  $\text{Mo}_x\text{W}_{1-x}\text{S}_2$  films. The high-resolution spectra of W 4f peaks are shown in Fig. 2g, whereas the doublets of W 4f<sub>5/2</sub> and 4f<sub>7/2</sub> are present in the W 4f spectrum at 37.6 eV and 35.5 eV, indicating the sulfur atom banded with the W atoms (W-S). Additionally, the peak intensity becomes stronger with the increase in the W content in the alloy film (Fig. 2g). The doublets of Mo 3d<sub>3/2</sub> and 3d<sub>5/2</sub> in the Mo 3d spectrum are at 232.0 and 228.8 eV, indicating the sulfur atom banded with the Mo atoms (Mo-S) (Fig. S10b, Supporting Information). The peaks at around 163.6 and 162.4 eV represent the S 2p<sub>1/2</sub> and S 2p<sub>3/2</sub>,

respectively (Fig. S10c, Supporting Information). As noticed, while W concentrations decreased from 1 to 0, the two peaks of W 4f softened and disappeared, indicating that the W concentrations decreased (Mo concentrations increased) with the decreased composition of  $x$  from 1 ( $\text{WS}_2$ ) to 0 ( $\text{MoS}_2$ ). Similar phenomenon can be found in the Mo 3d spectra. The composition of the  $\text{Mo}_x\text{W}_{1-x}\text{S}_2$  films was further estimated based on the XPS results. As shown in Fig. 2h, the calculated compositions are  $\text{WS}_2$ ,  $\text{Mo}_{0.22}\text{W}_{0.78}\text{S}_2$ ,  $\text{Mo}_{0.37}\text{W}_{0.63}\text{S}_2$ ,  $\text{Mo}_{0.56}\text{W}_{0.44}\text{S}_2$ ,  $\text{Mo}_{0.81}\text{W}_{0.19}\text{S}_2$ , and  $\text{MoS}_2$  with the theoretical  $x$  equal to 0, 0.2, 0.4, 0.6, 0.8, and 1, respectively. The calculated values are roughly consistent with the theoretical values, suggesting the considerably stoichiometric  $\text{MoS}_2$ ,  $\text{WS}_2$ , and their alloys.

### Electromechanical behavior of $\text{Mo}_x\text{W}_{1-x}\text{S}_2$ sensors

The strain sensing performance of the  $\text{Mo}_x\text{W}_{1-x}\text{S}_2$  sensor was examined by investigating the electrical response of the fabricated sensors under compressive and tensile strains induced by bending the sensors (insets in Figs. 3a and S11, Supporting Information). When an external force is applied, there is a displacement at the free end of the devices. A simplified cantilever model was used to evaluate the applied strains to the sensors, which can be calculated using the following equation (see details in “Materials and methods” section):

$$\varepsilon = \frac{3dt\Delta L(x)}{3Lx^2 - x^3} \quad (4)$$

where  $t$  and  $L$  are the thickness and length of the sensor,  $d$  is the distance of  $\text{Mo}_x\text{W}_{1-x}\text{S}_2$  alloys to the free end of the cantilever, and  $\Delta L(x)$  is the displacement of the cantilever at position  $x$ . The  $\text{Mo}_x\text{W}_{1-x}\text{S}_2$  patterns on the mica substrate were bent by a stepping motor with various displacements ( $\Delta L(x)$ ). The applied force induced in-plane pressure to  $\text{Mo}_x\text{W}_{1-x}\text{S}_2$  alloys, resulting in desired microstrains in the strain sensors.

The resistance values of the strain sensor were recorded using a digital multimeter and transmitted to a data acquisition system. Figure 3a shows the normalized resistance change ( $\Delta R/R_0$ ) of the sensor under various microstrains from  $-392$  to  $392 \mu\epsilon$ .  $\Delta R = R - R_0$  is the relative resistance change, where  $R_0$  and  $R$  are the resistance values of the sensor before and after being applied external force. It can be observed that there were sharp changes in the measured resistances when the strain was applied to the sensor. In specific, the resistance decreased under compressive strains. As expected, there was an increase in resistance when the sensor was bent outward. This is a typical piezoresistive behavior, which has been observed in  $\text{MoS}_2$  film<sup>24,33,34</sup>, phase-change film<sup>35</sup>, and polymer composite film<sup>36–39</sup>. In specific, there is a

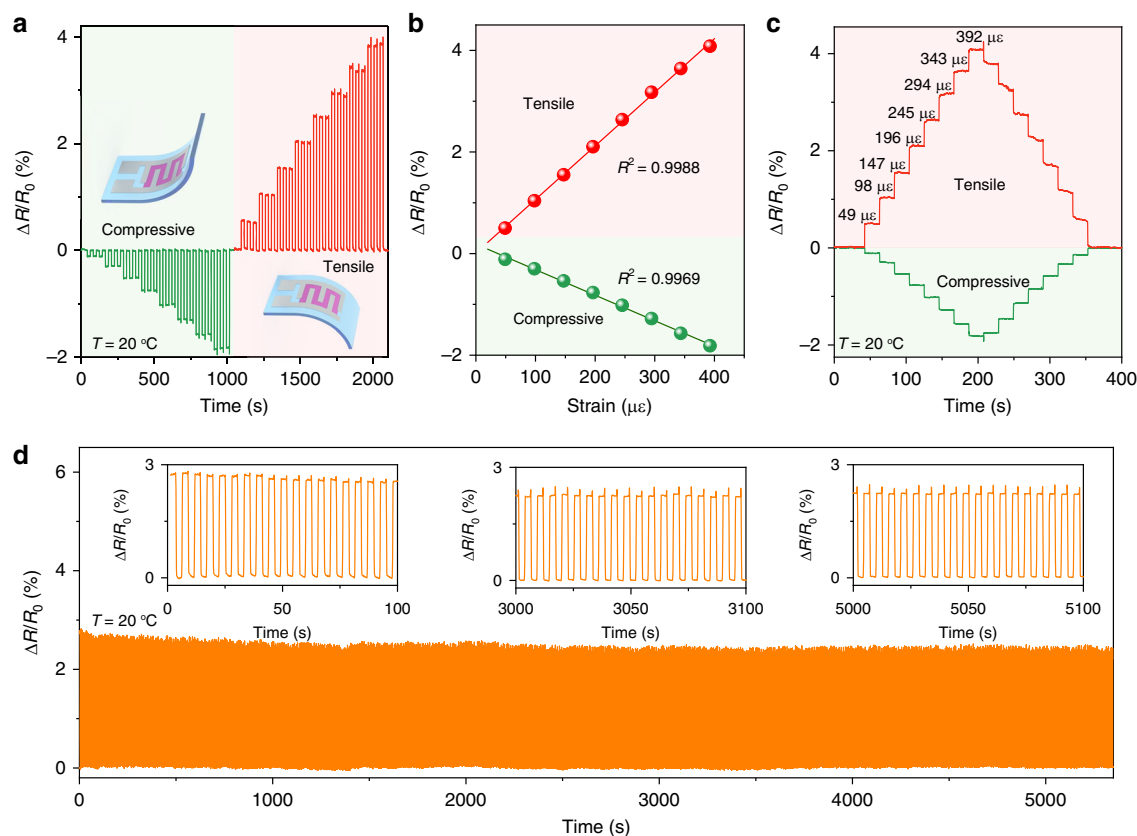


**Fig. 3** Electromechanical behavior of flexible  $\text{Mo}_x\text{W}_{1-x}\text{S}_2$  strain sensors at room temperature. **a** The normalized resistance of the strain sensor under compressive and tensile strains induced by inward bending and outward bending, respectively. Insets show the schematic of two bending modes. **b** Normalized resistance as a function of applied microstrains. The resistances are extracted from the values in **(a)** and averaged with a standard deviation. **c** Programmable and instantaneous resistance variation to different strains from 49 to 392  $\mu\epsilon$  during bending and releasing in compressive and tensile fashions. A holding time of 20 s was used at each strain value. All the tests were conducted at room temperature ( $20^\circ\text{C}$ ). **d** Dynamic cyclic test of the strain sensor at a strain of 294  $\mu\epsilon$  for over 1000 cycles

decreased atomic spacing in the  $\text{Mo}_x\text{W}_{1-x}\text{S}_2$  alloys under compressive strains, leading to a relatively higher electron density and a narrower band gap, which contributes to the increase in the electrical conductivity. In contrast, the enlarged atomic spacing and band gap under tensile strains results in the decreasing of electrical conductivity. Additionally, these changes were highly reversible, as confirmed by the consistent electrical response of the sensor stimulated by three times at each strain. Figure 3b compares the extracted resistance changes for the sensors with different strains. A high linearity was observed for both the compressive and tensile strains. The calculated strain sensitivity under compressive strains is  $-50.3$ . The normalized resistance change in the tensile mode is higher than that of the compressive mode, consistent with strain sensors in the literature.

The electrical response of the sensor to incremental strains is also evaluated by providing a stepping strain excitation with a step size of 49  $\mu\epsilon$  and unloaded back. The programmable change in strain was applied to

sensors in both compressive and tensile modes. As shown in Fig. 3c, there is a step change in the normalized resistance under both tensile and compressive states, which is consistent with the applied strains from 49 to 392  $\mu\epsilon$ , confirming the high repeatability, sensitivity, and fast response of the  $\text{Mo}_x\text{W}_{1-x}\text{S}_2$  sensor. Durability is important to strain sensors for long-term working. The fatigue life of the  $\text{Mo}_x\text{W}_{1-x}\text{S}_2$  sensor was investigated by conducting a cyclic test, in which a dynamic tensile strain of 294  $\mu\epsilon$  was applied to the sensor and then released at a frequency of 0.2 Hz. As shown in Fig. 3d, there is a stable response without noticeable degradation or attenuation during the cyclic loading and loading for more than 1000 cycles. The recorded resistance values and the amplitude of the electrical signals are roughly consistent throughout the repeated test cycles, indicating a high stability, reproducibility, and reliability of the sensor.

We also evaluate the sensing performance of the  $\text{Mo}_x\text{W}_{1-x}\text{S}_2$  sensor at high temperatures. Figure 4a, b shows the reversibility of the sensor in a tensile state at

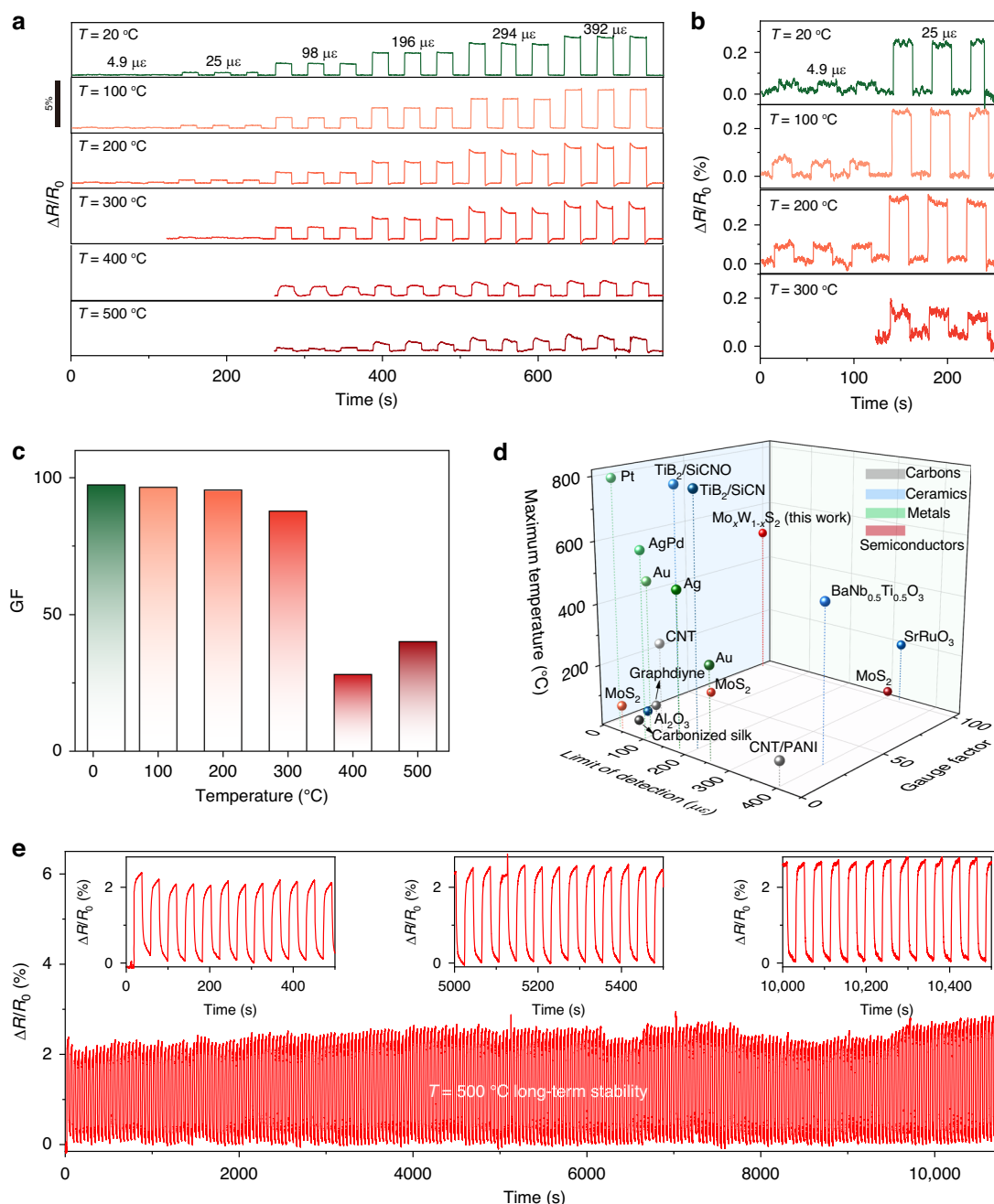


**Fig. 4** High-temperature strain sensing performance of the flexible  $\text{Mo}_x\text{W}_{1-x}\text{S}_2$  sensors. **a** Normalized resistance of the strain sensor responding to repetitive bending-and-releasing tests in the temperature regimes from 20 to 500 °C. Strains of 4.9 to 392  $\mu\epsilon$  are subjected to the sensor for three cycles at each strain. **b** Electrical response to microstrains of 4.9 and 25  $\mu\epsilon$  at temperatures of 20, 100, 200, and 300 °C. **c** Calculated GF of the sensor in the temperature range of 20–500 °C. **d** Benchmark of GF versus limit of detection with state-of-the-art high-temperature strain sensors based on metals, carbons, semiconductors, and ceramics. **e** Normalized resistance of the sensor under cyclic loading and unloading test with an applied strain of 392  $\mu\epsilon$  at 500 °C.

various temperatures from 20 to 500 °C. It can be observed that there are rapid variations in the normalized resistance when various microstrains from 4.9  $\mu\epsilon$  to 392  $\mu\epsilon$  are applied to the sensors. The resistances roughly recover to the initial values after unloading the strain.

There are no mechanical or electrical failures throughout the test, indicating the normal operation of the sensors at a temperature of up to 500 °C. Note that larger strains are not applied to the sensor due to the brittle mica substrate. It also shows that a subtle strain of about 4.9  $\mu\epsilon$  was

precisely detected at 20, 100, and 200 °C, indicating an ultra-low detection limit. Note that the detectable strains of the sensors at temperatures above 300 °C are higher than those at room temperature. Specifically, microstrain of 4.9  $\mu\epsilon$  is not detectable at temperatures above 300 °C, while the strain sensor can identify a minimal microstrain of 98  $\mu\epsilon$  at 400 °C and 500 °C. Additionally, the relative changes in resistance at higher temperatures (i.e., 400 and 500 °C) are about two times smaller than that at temperatures less than 300 °C (Fig. S11, Supporting Information). The degradation in sensing performance may be attributed to the relatively less sensitivity to strains at higher temperatures due to decreased mobility and large electron-phonon scattering effect<sup>40</sup>. Nevertheless, the detection limit is much lower than most high-temperature strain sensors in the literature<sup>5,41,42</sup>.

To investigate the sensitivity of the  $\text{Mo}_x\text{W}_{1-x}\text{S}_2$  strain sensor, we calculate the GF. As shown in Figs. 4c and S11, Supporting Information, the GFs maintain relatively stable values at temperatures up to 300 °C. Specifically, the GFs of the sensor are 97.4 and 87.8 at temperatures of 20 °C and 300 °C, respectively. There is performance degradation in the GFs at temperatures higher than 400 °C, whereas the values are 28.1 and 40.1 at 400 °C and 500 °C, respectively. The slightly decreased strain sensitivity is consistent with high-temperature strain sensors in the literature<sup>5,43</sup>. Despite the slightly degraded GFs, our sensor retains its operation at 500 °C, showing its tolerance to high temperatures.

It is known that developing strain gauges with high sensitivity, low detection limit, and wide temperature range are crucial for high-temperature applications. The collective sensing performance of our  $\text{Mo}_x\text{W}_{1-x}\text{S}_2$  strain sensors is compared with other functional materials-based high-temperature strain sensors, such as metals<sup>5,7,44</sup>, semiconductors<sup>27,45,46</sup>, and carbons<sup>42,47,48</sup>. Our  $\text{Mo}_x\text{W}_{1-x}\text{S}_2$  sensor exhibits state-of-the-art levels in GF, detection limit, and operation temperatures (Fig. 4d and Table 1).

Specifically, the noble metals- and inorganic ceramics-based strain sensors can detect relatively low strains at temperatures even higher than 600 °C. However, their sensitivity to external strains is typically low, resulting in low GFs. In contrast, strain sensors made of semiconductors (e.g.,  $\text{MoS}_2$ ), and carbons (e.g., carbon nanotubes (CNT)), typically exhibit higher GF but with lower operation temperatures. Our  $\text{Mo}_x\text{W}_{1-x}\text{S}_2$ -based sensors process superior strain sensing performance, such as high sensitivity, low detection limit, and wide temperature regime (20–500 °C). The strain sensitivity of our sensor is one order of magnitude higher than metallic strain sensors and carbon-based sensors. Simultaneously, the  $\text{Mo}_x\text{W}_{1-x}\text{S}_2$ -based sensor has the lowest detection limit, which can distinguish a microstrain down to 4.9  $\mu\epsilon$ .

**Table 1 Comparison of strain sensors**

Sensing materials	LOD ( $\mu\epsilon$ )	Strain-GF	Temperature range (°C)	Ref.
Pt	29.9	2.55	30–800	5
Au	250	2.26	200–300	59
AgPd	100	1.25	600	7
Ag	175	3.15	500	43
$\text{BaNb}_{0.5}\text{Ti}_{0.5}\text{O}_3$	700	27.5	20	60
AlN	100	0.00192	15.4–250	61
$\text{TiB}_2/\text{SiCN}$	200	7.12	25–800	62
CNT	110	4.13	0–300	42
CNT/PANI	400	1.77	25–80	48
MXene-Graphene	120	3.7	10–200	63
PANI	5000	18.28	40–110	64
$\text{MoS}_2$	50	51.2	RT	45
$\text{MoS}_2$	30	1.8	20–70	27
$\text{MoS}_2$	NA	NA	30–80	23
$\text{MoS}_2$	NA	47.2	RT	34
<b><math>\text{Mo}_x\text{W}_{1-x}\text{S}_2</math></b>	<b>4.9</b>	<b>97.4</b>	<b>20–500</b>	<b>This work</b>

LOD limit of detection, CNT carbon nanotubes, PANI polyaniline

Owing to the capability for subtle strain identification, our sensor is expected to bring various potential applications, such as pulse and respiration detecting, robotic controlling, and wound healing monitoring. It could be attributed to the wrinkled microstructures of the  $\text{Mo}_x\text{W}_{1-x}\text{S}_2$  films and the high adhesion between the film and substrate. In specific, the wrinkled structures are expected to introduce more defects or free-standing regions in the  $\text{Mo}_x\text{W}_{1-x}\text{S}_2$  films, making the nanoscale films more fragile than their flattened counterparts<sup>49–51</sup>, benefiting the high electrical response under small strains. This is verified by the relatively smaller GFs of strain sensor (−35.2 at 20 °C) based on flat  $\text{Mo}_x\text{W}_{1-x}\text{S}_2$  films (Fig. S12, Supporting Information), as compared to the strain sensor with wrinkled structures (−50.3 at 20 °C). Additionally, some minuscule cracks are expected to be generated in the laser writing process, enabling an enhanced sensitivity and detectable strain range<sup>52,53</sup>. Moreover, compared to pure  $\text{MoS}_2$ ,  $\text{Mo}_x\text{W}_{1-x}\text{S}_2$  alloys may retain more stable electrical properties over a wide range of temperatures<sup>54,55</sup>.

In addition to the sensitivity, detection limit, and operation temperature, the response time to rapid strain loading and unloading was another parameter of high-performance strain sensors. We noted a sharp and rapid increase in the normalized resistance (0.49 s) when a



microstrain is applied to the sensor at 300 °C. After removing the strain, the resistance recovered to the initial value within 0.41 s (Fig. S13, Supporting Information). The short response and recovery times are well maintained over a wide temperature regime from 20 to 200 °C. In specific, the response times of the sensor are 0.45, 0.45, and 0.46 s at 20, 100, and 200 °C, respectively. The recovery times of the sensor are 0.41, 0.39, and 0.42 s at 20, 100, 200 °C, respectively. At temperatures over 400 °C, there is a relatively slower response to external strains. The response and recovery times are 0.7 and 0.46 s at 400 °C, while the times increase slightly to 0.73 and 0.5 s at 500 °C. Nevertheless, the response time of the proposed  $\text{Mo}_x\text{W}_{1-x}\text{S}_2$  sensors is still lower than most reported high-temperature strain sensors<sup>4,56,57</sup>.

The electrical reliability of the  $\text{Mo}_x\text{W}_{1-x}\text{S}_2$  sensor at high temperatures was also investigated by cyclic loading and unloading a strain of 392  $\mu\epsilon$  to the sensor. Figure 4e shows that the sensor responses at the initial, medium, and last cycles at 500 °C are roughly consistent. The  $\text{Mo}_x\text{W}_{1-x}\text{S}_2$  sensor retains relatively stable output throughout the 250 tensile cycles at a large strain of 392  $\mu\epsilon$  and high temperature of 500 °C. Additionally, the  $\text{Mo}_x\text{W}_{1-x}\text{S}_2$  sensor can sustain the electrical and sensing properties for 3 h (11000 s) at 500 °C, indicating the strong tolerance to high temperature. The resistance slightly increases by 12% from the initial status to the end (insets in Fig. 4e), which can be attributed to several potential reasons. From material's perspective, fatigue or creep may occur in both flexible substrate and alloy film due to possible irreversible deformations under high temperature. Additionally, there may have microcracks or unnoticeable delamination at the interface in the cyclic bending test at high temperature, resulting in increased contact resistance. Moreover, the mismatch in thermal expansion coefficient between the mica substrate and alloy film will generate internal stress during the cyclic bending, causing the signal inconsistency from the initial status to the end. Nevertheless, the strain sensor can operate reliably at a high temperature of 500 °C for more than 3 h, implying the potential application in high-temperature environments. We also evaluate the mechanical behavior of the mica-based flexible sensor by applying tensile strain to the sensor. It is found that the sensor exhibits a tensile strength of about 23 MPa at a tensile strain of 0.25% (Fig. S14, Supporting Information), offering high stability for the flexible sensors.

### Integrated wireless acoustic recognition system

Owing to the high sensitivity over a broad temperature range, the flexible  $\text{Mo}_x\text{W}_{1-x}\text{S}_2$  sensor can be utilized for monitoring small strains in high-temperature environments. As a proof of concept, we demonstrate the application of the  $\text{Mo}_x\text{W}_{1-x}\text{S}_2$  sensor in the field of acoustic

diagnosis, which always involves distinguishing tiny signals under extreme temperature conditions. Figure 5a, b shows the developed vibration identification system that enables the real-time frequency detection of tuning fork at 300 °C for high-temperature acoustic applications. The systems comprise three major components, including the strain sensing based on  $\text{Mo}_x\text{W}_{1-x}\text{S}_2$  films, a self-developed bleeder circuit, and an oscilloscope (Fig. 5a). The flexible  $\text{Mo}_x\text{W}_{1-x}\text{S}_2$  sensor is attached to the surface of tuning forks for recording vibration signals with various frequencies. The bleeder circuit includes a voltage divider module (Fig. S15, Supporting Information), which is used to power the  $\text{Mo}_x\text{W}_{1-x}\text{S}_2$  sensor by providing a direct current voltage. The sampled voltage data is then quantized and encoded through the circuit. The oscilloscope connects both ends of the sensor electrodes and the bleeder circuit to record the voltage variation across the thin-film sensor in real-time. The obtained voltage values are directly displayed on the oscilloscope. To improve the data processing efficiency, we have also developed another wireless vibration identification system, comprising a home-made printed circuit board for data collection and pre-processing, a WiFi module for wireless data transfer, and a computer with an interface for wave analysis<sup>58</sup>, as schematically illustrated in Fig. 5a. Different from the bleeder circuit, the wireless system record resistance values of the  $\text{Mo}_x\text{W}_{1-x}\text{S}_2$  sensor induced by the vibration of tuning forks. These resistive signals are firstly pre-processed by a microcontroller unit and converted into digital signals by an analog-to-digital converter. The converted digital signals are then wirelessly transferred to a computer. An oscilloscope module is implemented in the computer to display the converted signal through a developed interface.

Figure 5c shows the real-time voltage change of the flexible  $\text{Mo}_x\text{W}_{1-x}\text{S}_2$  sensor when contacting tuning forks with vibration frequencies of 32, 64, and 128 Hz at an input voltage of 5 V. The sensor can detect and identify all those vibrations. The amplitude values of the signals obtained during the test are consistent with the original inputs. The embedded graphs show the recorded voltage signals within 0.1 s, indicating a high fidelity of the data, which verifies that the flexible  $\text{Mo}_x\text{W}_{1-x}\text{S}_2$  sensor can respond accurately to high-frequency signals up to 128 Hz. Note that there is weak response when a higher vibration frequency (>128 Hz) is applied to the strain sensor, which can be resolved by optimizing the response time and strain sensitivity through material and structure design. The corresponding Fourier transform result show that there is a sharp peak at 32 Hz in the recorded signals from the sensor attached to the tuning fork with an intrinsic frequency of 32 Hz (Fig. 5c). Similarly, a peak locating at 64 Hz in Fig. 5d is consistent with the intrinsic frequency of the tuning fork, while there is a sharp peak at 128 Hz in the Fourier transformed curve in Fig. 5e when

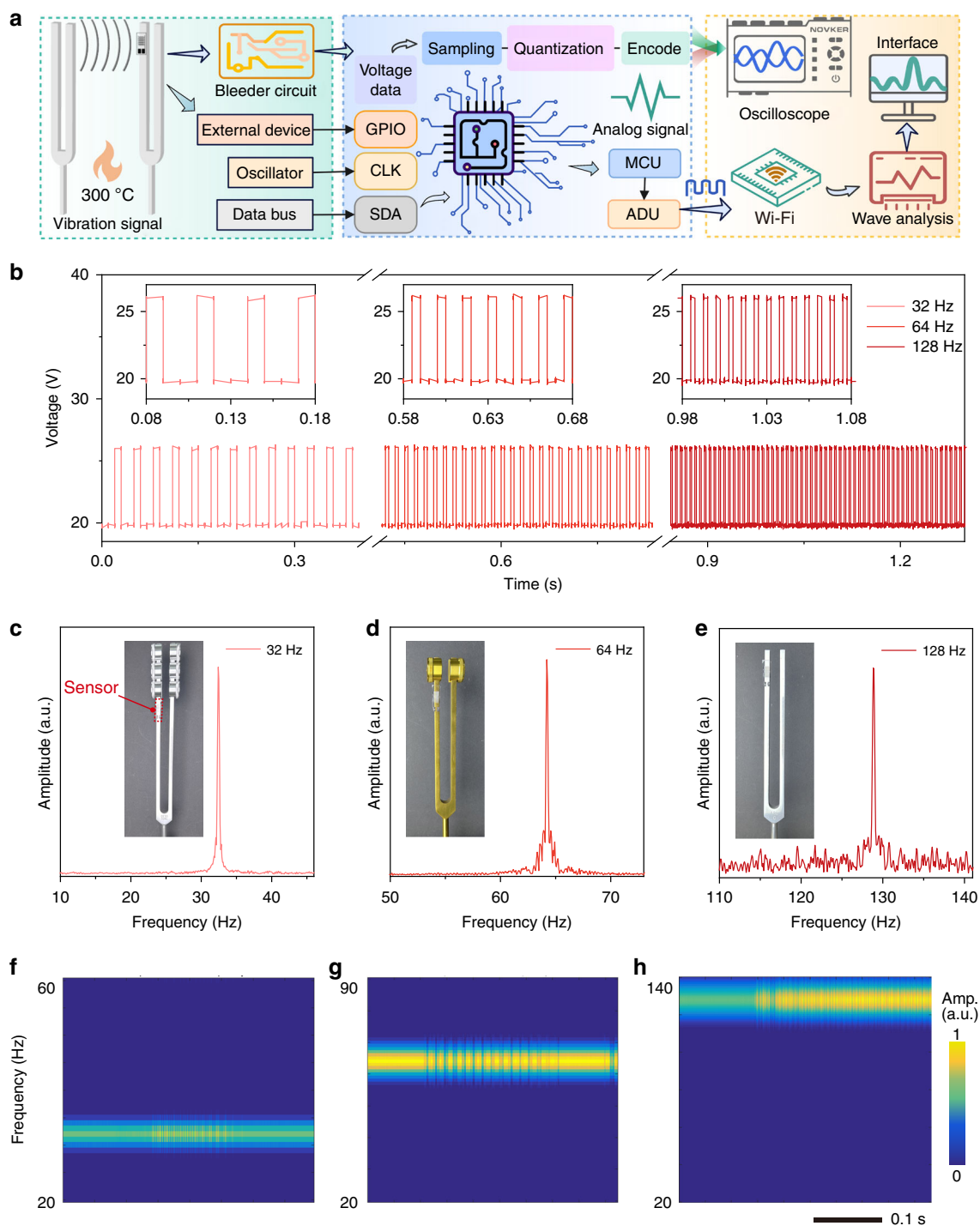


**Fig. 5** Demonstration of the flexible  $\text{Mo}_x\text{W}_{1-x}\text{S}_2$  sensor in high-temperature vibration identification system under 300 °C. **a** Schematic illustration showing the construction of the system, including  $\text{Mo}_x\text{W}_{1-x}\text{S}_2$ -based microstrain sensing, main control printed circuit board, self-developed voltage acquisition bleeder circuit, and an oscilloscope with a wave analysis module. **b** Recorded voltage response of the sensor to various vibration frequencies of 32, 64, and 128 Hz. **c–e** The corresponding frequency spectrums of the signals in **(b)**. Insets show the photographs of the tuning forks with various frequencies from 32 Hz to 128 Hz. **f–h** The corresponding time-frequency spectrograms of the signals in **(b)**

the intrinsic frequency of the tuning forks is 128 Hz. We further conduct spectrum analysis of the recorded signals. Figure 5f–h show the time-frequency domain analysis of the output voltages for the flexible sensors contacting with tuning forks at frequencies of 32, 64, and 128 Hz, respectively. The flexible  $\text{Mo}_x\text{W}_{1-x}\text{S}_2$  sensor can clearly distinguish the frequency of the tuning forks through the sampling and analysis of high-frequency signals, confirming that the sensor can acquire high-frequency micro-strain signals with high accuracy and reliability in high-temperature environments.

## Conclusion

In this study, we developed a direct laser writing approach for the custom design and direct fabrication of  $\text{Mo}_x\text{W}_{1-x}\text{S}_2$  films-based flexible strain sensors. Through this rapid and convenient method, we can regulate and precisely control the compositions, thicknesses, and shapes of the  $\text{Mo}_x\text{W}_{1-x}\text{S}_2$  alloy films during the laser annealing process. The sensing element can detect a low microstrain down to  $4.9\ \mu\epsilon$ , and the GFs of about 90 are well retained up to  $300\ ^\circ\text{C}$ , both of which are the best compared to the state-of-the-art benchmarks in the literature. Moreover, the sensors demonstrate superior mechanical and thermal stability with no noticeable degradation in sensing performance or structure failure upon repetitive bending and releasing cycles at  $500\ ^\circ\text{C}$  for 3 h. The proposed strategy for synthesizing  $\text{Mo}_x\text{W}_{1-x}\text{S}_2$  alloy films and manufacturing flexible sensors demonstrates promising applications in the design and realization of flexible electronics operating at high temperatures for harsh environments.

Despite the superior strain sensing performance of  $\text{Mo}_x\text{W}_{1-x}\text{S}_2$  alloy films-based sensors, several critical challenges remain that may hinder their potential applications. First, the sensing performance degrades at elevated temperatures. Second, the strain sensitivity remains insufficient for detecting nanoscale mechanical deformations in applications such as biomedical pulse monitoring or high-frequency vibration diagnosis. Third, the relatively large response and recovery times impede real-time detection of high-frequency dynamic strains, limiting their application in fast-response systems.

To address these challenges, several strategic approaches can be conducted. From material's perspective, introducing additional transition metals to form high-entropy sulfides is expected to enhance thermal stability. Interface between the sensing film and flexible substrate should be enhanced by applying advanced surface treatments or introducing interlayers to improve the adhesion. Serpentine or fractal designs can be employed to reduce stress concentration at high temperature. Through these strategies, both strain sensitivity and high-temperature stability of flexible strain sensors are expected to be enhanced.

## Acknowledgements

This work was financially supported by the National Natural Science Foundation of China (No. 62288102, 62371397, 62304182, and 62471396), the Fundamental Research Funds for the Central Universities, the Young Talent Fund of Xi'an Association for Science and Technology (No. 959202413089), Engineering Research Center of Flexible Electronics, Universities of Shaanxi Province, and Open Test Funding Project from Analytical & Testing Center of Northwestern Polytechnical University (No. 2023T008).

## Author details

<sup>1</sup>State Key Laboratory of Flexible Electronics (LoFE) & Institute of Flexible Electronics (IFE), Northwestern Polytechnical University, Xi'an 710072, China. <sup>2</sup>Shaanxi Key Laboratory of Flexible Electronics, Northwestern Polytechnical University, Xi'an 710072, China. <sup>3</sup>MIT Key Laboratory of Flexible Electronics (KLoFE), Northwestern Polytechnical University, Xi'an 710072, China. <sup>4</sup>Henan Institute of Flexible Electronics (HIFE) and School of Flexible Electronics (SoFE), Henan University, Zhengzhou 450046, China. <sup>5</sup>State Key Laboratory of Flexible Electronics (LoFE) and Institute of Advanced Materials (IAM), Nanjing University of Posts & Telecommunications, Nanjing 210023, China. <sup>6</sup>State Key Laboratory of Flexible Electronics (LoFE) and Institute of Advanced Materials (IAM), Nanjing Tech University, Nanjing 211800, China

## Author contributions

**Xexin Wang:** methodology, data curation, formal analysis, writing—original draft. **Hanxin Wang:** methodology, data curation, formal analysis. **Xiaoshan Zhang:** methodology, data curation. **Yingzhe Li:** methodology, validation, data curation. **Yilin Zhou:** data curation. **Manzhang Xu:** supervision, formal analysis, writing—original draft, writing—review & editing. **Weiwei Li:** supervision, project administration, funding acquisition, formal analysis, writing—original draft, writing—review & editing. **Lu Zheng:** supervision, project administration, funding acquisition. **Xuewen Wang:** supervision, project administration, funding acquisition, writing—review & editing. **Wei Huang:** supervision.

## Data availability

The datasets generated during and/or analyzed during the current study are available from the corresponding author on reasonable request.

## Conflict of interest

The authors declare no competing interests.

**Supplementary information** The online version contains supplementary material available at <https://doi.org/10.1038/s41378-025-01014-1>.

Received: 19 February 2025 Revised: 13 May 2025 Accepted: 1 July 2025  
Published online: 19 August 2025

## References

- Jiang, H., Zheng, L., Liu, Z. & Wang, X. Two-dimensional materials: from mechanical properties to flexible mechanical sensors. *InfoMat* **2**, 1077–1094 (2020).
- Gleich, B., Schmale, I., Nielsen, T. & Rahmer, J. Miniature magneto-mechanical resonators for wireless tracking and sensing. *Science* **380**, 966–971 (2023).
- He, R. et al. Flexible miniaturized sensor technologies for long-term physiological monitoring. *NPJ Flex. Electron* **6**, 20 (2022).
- Chen, G. et al. Conformal fabrication of thick film platinum strain gauge via error regulation strategies for in situ high-temperature strain detection. *ACS Appl. Mater. Interfaces* **16**, 966–974 (2024).
- Wu, C. et al. Multilayer co-sintered Pt thin-film strain gauge for high-temperature applications. *Surf. Coat. Technol.* **459**, 129380 (2023).
- Zeng, Y. et al. All-three-dimensionally-printed AgPd thick-film strain gauge with a glass-ceramic protective layer for high-temperature applications. *ACS Appl. Mater. Interfaces* **15**, 48395–48405 (2023).
- Wu, C. et al. AgPd thin-film strain gauges fabricated by direct writing for high-temperature application. *IEEE Sens. J.* **22**, 22473–22478 (2022).
- Liu, Z. et al. Flexible temperature sensor with high sensitivity ranging from liquid nitrogen temperature to  $1200\ ^\circ\text{C}$ . *Int. J. Extrem. Manuf.* **5**, 015601 (2023).

9. Liu, Z. et al. Effect of nitrogen partial pressure on the piezoresistivity of magnetron sputtered ITO thin films at high temperatures. *Appl. Surf. Sci.* **608**, 155292 (2023).
10. Kang, M. et al. Wireless graphene-based thermal patch for obtaining temperature distribution and performing thermography. *Sci. Adv.* **8**, eabm6693 (2022).
11. Lin, M. et al. A high-performance, sensitive, wearable multifunctional sensor based on rubber/CNT for human motion and skin temperature detection. *Adv. Mater.* **34**, 2107309 (2022).
12. Kireev, D. et al. Continuous cuffless monitoring of arterial blood pressure via graphene bioimpedance tattoos. *Nat. Nanotechnol.* **17**, 864–870 (2022).
13. Li, H.-Y., Zhao, S.-N., Zang, S.-Q. & Li, J. Functional metal–organic frameworks as effective sensors of gases and volatile compounds. *Chem. Soc. Rev.* **49**, 6364–6401 (2020).
14. Yang, X. et al. Wet-adhesive on-skin sensors based on metal-organic frameworks for wireless monitoring of metabolites in sweat. *Adv. Mater.* **34**, 2201768 (2022).
15. Kwon, C. et al. Multi-functional and stretchable thermoelectric Bi<sub>2</sub>Te<sub>3</sub> fabric for strain, pressure, and temperature-sensing. *Adv. Funct. Mater.* **33**, 2300092 (2023).
16. Manzeli, S., Ovchinnikov, D., Pasquier, D., Yazyev, O. V. & Kis, A. 2D transition metal dichalcogenides. *Nat. Rev. Mater.* **2**, 17033 (2017).
17. Pinilla, S., Coelho, J., Li, K., Liu, J. & Nicolosi, V. Two-dimensional material inks. *Nat. Rev. Mater.* **7**, 717–735 (2022).
18. Kim, Y. et al. Recent advances in functionalization and hybridization of two-dimensional transition metal dichalcogenide for gas sensor. *Adv. Eng. Mater.* **26**, 2301063 (2024).
19. Zheng, L. et al. Recent progress of flexible electronics by 2D transition metal dichalcogenides. *Nano Res.* **15**, 2413–2432 (2022).
20. Huang, Y. et al. Van der Waals coupled organic molecules with monolayer MoS<sub>2</sub> for fast response photodetectors with gate-tunable responsivity. *ACS Nano* **12**, 4062–4073 (2018).
21. Abnavi, A. et al. Flexible high-performance photovoltaic devices based on 2D MoS<sub>2</sub> diodes with geometrically asymmetric contact areas. *Adv. Funct. Mater.* **33**, 2210619 (2023).
22. Gui, T. et al. In-situ fabrication of PtSe<sub>2</sub>/MoS<sub>2</sub> van der Waals heterojunction for self-powered and broadband photodetector. *Mater. Des.* **238**, 112722 (2024).
23. Daus, A. et al. Fast-response flexible temperature sensors with atomically thin molybdenum disulfide. *Nano Lett.* **22**, 6135–6140 (2022).
24. Li, W. et al. Microsecond-scale transient thermal sensing enabled by flexible Mo<sub>1-x</sub>W<sub>x</sub>S<sub>2</sub> alloys. *Research* **7**, 0452 (2024).
25. Xu, M. et al. Programmable patterned MoS<sub>2</sub> film by direct laser writing for health-related signals monitoring. *Isience* **24**, 103313 (2021).
26. Park, M. et al. MoS<sub>2</sub>-based tactile sensor for electronic skin applications. *Adv. Mater.* **28**, 2556–2562 (2016).
27. Li, W. et al. Large-scale ultra-robust MoS<sub>2</sub> patterns directly synthesized on polymer substrate for flexible sensing electronics. *Adv. Mater.* **35**, 2207447 (2023).
28. Hu, Y. et al. One-step growth of centimeter-scale doped multilayer MoS<sub>2</sub> films by pulsed laser-induced synthesis. *J. Mater. Chem. C* **8**, 6900–6905 (2020).
29. Xu, M. et al. Reconfiguring nucleation for CVD growth of twisted bilayer MoS<sub>2</sub> with a wide range of twist angles. *Nat. Commun.* **15**, 562 (2024).
30. Xu, M. et al. CVD synthesis of twisted bilayer WS<sub>2</sub> with tunable second harmonic generation. *Adv. Mater.* **36**, 2313638 (2024).
31. Yu, H. et al. Spatially graded millimeter sized Mo<sub>1-x</sub>W<sub>x</sub>S<sub>2</sub> monolayer alloys: synthesis and memory effect. *ACS Appl. Mater. Interfaces* **13**, 44693–44702 (2021).
32. Averchenko, A. V. et al. Laser-enabled localized synthesis of Mo<sub>1-x</sub>W<sub>x</sub>S<sub>2</sub> alloys with tunable composition. *Mater. Today Adv.* **17**, 100351 (2023).
33. Manzeli, S., Allain, A., Ghadimi, A. & Kis, A. Piezoresistivity and strain-induced band gap tuning in atomically thin MoS<sub>2</sub>. *Nano Lett.* **15**, 5330–5335 (2015).
34. Luo, L. et al. Ultra-low power consumption flexible sensing electronics by dendritic bilayer MoS<sub>2</sub>. *InfoMat* **6**, e12605 (2024).
35. Wang, Z. et al. Highly sensitive integrated flexible tactile sensors with piezo-resistive Ge<sub>2</sub>Sb<sub>2</sub>Te<sub>5</sub> thin films. *NPJ Flex. Electron.* **2**, 17 (2018).
36. Cheng, Y., Jiang, B., Chaemchuen, S., Verpoort, F. & Kou, Z. Advances and challenges in designing MXene quantum dots for sensors. *Carbon Neutralization* **2**, 213–234 (2023).
37. Li, C. et al. Deep learning model coupling wearable bioelectric and mechanical sensors for refined muscle strength assessment. *Research* **7**, 0366 (2024).
38. Gao, J. et al. Disposable and flexible smart electronic tapes for long-term biopotential monitoring. *NPJ Flex. Electron.* **9**, 6 (2025).
39. Li, Y. et al. Breaking the saturation of sensitivity for ultrawide range flexible pressure sensors by soft-strain effect. *Adv. Mater.* **36**, 2405405 (2024).
40. Jiang, C., Rumyantsev, S. L., Samnakay, R., Shur, M. S. & Balandin, A. A. High-temperature performance of MoS<sub>2</sub> thin-film transistors: direct current and pulse current-voltage characteristics. *J. Appl. Phys.* **117**, 064301 (2015).
41. Xu, L. et al. In situ laser fabrication of polymer-derived ceramic composite thin-film sensors for harsh environments. *ACS Appl. Mater. Interfaces* **14**, 12652–12661 (2022).
42. Zou, S., Wang, Y., Li, D., Zhang, Y. & Cai, G. Facile and scalable fabrication of stretchable flame-resistant yarn for temperature monitoring and strain sensing. *Chem. Eng. J.* **450**, 138465 (2022).
43. Rahman, M. T., Moser, R., Zbib, H. M., Ramana, C. V. & Panat, R. 3D printed high performance strain sensors for high temperature applications. *J. Appl. Phys.* **123**, 024501 (2018).
44. Shu, L. et al. High-temperature SAW wireless strain sensor with langasite. *Sensors* **15**, 28531–28542 (2015).
45. Park, S. et al. Layer-selective synthesis of MoS<sub>2</sub> and WS<sub>2</sub> structures under ambient conditions for customized electronics. *ACS Nano* **14**, 8485–8494 (2020).
46. Rana, V. et al. A highly sensitive wearable flexible strain sensor based on polycrystalline MoS<sub>2</sub> thin film. *Nanotechnology* **31**, 385501 (2020).
47. Cai, Y. et al. Graphdiyne-based nanofilms for compliant on-skin sensing. *ACS Nano* **16**, 16677–16689 (2022).
48. Jung, G. et al. Temperature-tolerant flexible supercapacitor integrated with a strain sensor using an organohydrogel for wearable electronics. *Chem. Eng. J.* **450**, 138379 (2022).
49. Zhao, Y. et al. Large-area transfer of two-dimensional materials free of cracks, contamination and wrinkles via controllable conformal contact. *Nat. Commun.* **13**, 4409 (2022).
50. Zhang, Z. et al. Rosin-enabled ultraclean and damage-free transfer of graphene for large-area flexible organic light-emitting diodes. *Nat. Commun.* **8**, 14560 (2017).
51. Li, X. et al. Large-area synthesis of high-quality and uniform graphene films on copper foils. *Science* **324**, 1312–1314 (2009).
52. Guo, Y. et al. Multifunctional hydrogel sensor with curved macro cracks: a strategy for high sensitivity and wide detection range. *Adv. Funct. Mater.* **33**, 2306820 (2023).
53. Wang, L. et al. Crack sensing of cardiomyocyte contractility with high sensitivity and stability. *ACS Nano* **16**, 12645–12655 (2022).
54. Gao, J. et al. Transition-metal substitution doping in synthetic atomically thin semiconductors. *Adv. Mater.* **28**, 9735–9743 (2016).
55. Gao, H. et al. Tuning electrical conductance of MoS<sub>2</sub> monolayers through substitutional doping. *Nano Lett.* **20**, 4095–4101 (2020).
56. Lin, F. et al. ZrB<sub>2</sub>/SiCN thin-film strain gauges for in-situ strain detection of hot components. *Micromachines* **13**, 1467 (2022).
57. Ma, H. et al. Large area and flexible flexion sensing matrix for detection of strain distribution in bendable and curved surface. *ACS Sens* **10**, 4896–4905 (2025).
58. Kong, L. et al. Wireless technologies in flexible and wearable sensing: from materials design, system integration to applications. *Adv. Mater.* **36**, 2400333 (2024).
59. Lee, C.-Y., Shen, C.-C., Lee, S.-J., Chiu, C.-W. & Lin, H.-T. Real-time microscopic monitoring of temperature and strain on the surface of magnesium hydrogen storage tank by high temperature resistant flexible integrated microsensor. *Int. J. Hydrog. Energy* **47**, 12815–12821 (2022).
60. Yang, C. et al. A flexible strain sensor of Ba(Ti, Nb)O<sub>3</sub>/mica with a broad working temperature range. *Adv. Mater. Technol.* **4**, 1900578 (2019).
61. Dou, S. High-temperature high-sensitivity AlN-on-SOI Lamb wave resonant strain sensor. *AIP Adv.* **8**, 065315 (2018).
62. Wu, C. et al. TiB<sub>2</sub>/SiCN thin-film strain gauges fabricated by direct writing for high-temperature application. *IEEE Sens. J.* **22**, 11517–11525 (2022).
63. Saeidi-Javash, M. et al. All-printed MXene–graphene nanosheet-based bimodal sensors for simultaneous strain and temperature sensing. *ACS Appl. Electron. Mater.* **3**, 2341–2348 (2021).
64. Ge, G. et al. Muscle-inspired self-healing hydrogels for strain and temperature sensor. *ACS Nano* **14**, 218–228 (2020).